OPTICS

Multiscale dynamical symmetries and selection rules in nonlinear optics

Gavriel Lerner[1,2]*, Ofer Neufeld[1,2,3], Liran Hareli[4], Georgiy Shoulga[4], Eliayu Bordo[1,2], Avner Fleischer[5,6], Daniel Podolsky[1], Alon Bahabad[4], Oren Cohen[1,2]*

Symmetries and their associated selection rules are extremely useful in many fields of science. For systems of electromagnetic (EM) fields interacting with matter, the symmetries of matter and the EM fields' time-dependent polarization determine the properties of the nonlinear responses, and they can be facilitated for controlling light emission and enabling ultrafast symmetry breaking spectroscopy of various properties. Here, we formulate a general theory that describes the macroscopic and microscopic dynamical symmetries (including quasicrystal-like symmetries) of EM vector fields, revealing many previously unidentified symmetries and selection rules in light-matter interactions. We demonstrate an example of multiscale selection rules experimentally in the framework of high harmonic generation. This work paves the way for novel spectroscopic techniques in multiscale systems and for imprinting complex structures in extreme ultraviolet–x-ray beams, attosecond pulses, or the interacting medium itself.

INTRODUCTION

Symmetry is regularly used to derive conservation laws and selection rules in interacting systems (*1*). In the field of nonlinear optics, symmetries are standardly used to determine whether a particular nonlinear process is allowed or forbidden according to the medium's point group (*2*, *3*). Recently, a more general group theory was developed to describe the symmetries of the electromagnetic (EM) field's time-dependent polarization, named dynamical symmetries (DSs) (*4*). Such DSs and their associated selection rules have been applied to shaping the waveforms of extreme ultraviolet (XUV) and x-ray radiation emitted from high harmonic generation (HHG) (*5*–*7*) and have enabled ultrafast symmetry breaking spectroscopy of molecular (*8*, *9*) and solid orientation (*10*), molecular symmetries (*9*), and chirality (*11*, *12*). However, this theory of DSs is local (operating solely on a microscopic scale) (*13*) and, thus, fully neglects light's macroscopic structure. Moreover, it does not account for composite microscopic-macroscopic (multiscale) DSs.

Here, we formulate a general theory for EM fields and their interactions with matter, where the multiscale symmetries of the full light-matter Hamiltonian are analyzed. We describe spatiotemporal DSs as generalized unitary transformations and study systematically all possible symmetry operations that close under group multiplication. Various combinations of EM fields are cataloged into different groups that are composed of one or more DSs. We assign each DS an associated selection rule that indicates the allowed frequencies, polarizations, momenta, and angular momenta of the harmonic emission. Our theory generalizes many previous results, such as complex structured XUV emission generated by spatiotemporal structure beams in the beams' longitudinal axis (*14*–*17*) or profile (*5*–*7*, *18*, *19*). We also found previously unidentified types of symmetries, including simultaneous spin-orbit angular momentum conservation, and periodic (*20*) and aperiodic (*21*) space-time crystals of a vector field. We explore several new multiscale DSs numerically and experimentally in the framework of HHG to demonstrate the richness of this approach for light-matter interactions.

We begin by describing the multiscale DSs of an EM vector field, which are combinations of temporal, microscale, and macroscale spatial building blocks. Then, we derive a general equation that determines the selection rules of the polarization and frequencies (temporal and spatial) of generated harmonics.

RESULTS

Multiscale symmetries

We analyze here the symmetries of electric vector fields; however, the theory is general and can be applied to the symmetries of time-periodic Hamiltonians and other equations of motion, as we show in later sections. The basic entity we explore is the vector field

$$\vec{E} = \vec{E}(\vec{R}, t) = \vec{E}(\vec{X}) \quad (1)$$

where $\vec{R}$ denotes the spatial dependence of this field and t represents its temporal dependence. For brevity, we define a general spatiotemporal coordinate vector, $\vec{X}$. It is beneficial to separate the three types of degrees of freedom (DOFs) of $\vec{E}(\vec{X})$: (i) As a vector field, $\vec{E}(\vec{X})$ has three independent polarization components—E_x, E_y, and E_z. We denote these as microscopic DOFs of the field, as they reflect its intrinsic local structure in a given spatial location. (ii) $\vec{E}$ may depend on three spatial coordinates. We denote these as macroscopic DOFs, as they reflect the spatial structure of the field. (iii) $\vec{E}$ depends on the time coordinate. A symmetry of $\vec{E}$ is an operation that keeps it invariant; hence, a complex spatiotemporal operation $\hat{G}$ is a symmetry if $\hat{G}\vec{E} = \vec{E}$. The "order" n of this operation is the number of times it needs to

[1]Physics Department, Technion – Israel Institute of Technology, Haifa, Israel. [2]Solid State Institute, Technion – Israel Institute of Technology, Haifa, Israel. [3]Max Planck Institute for the Structure and Dynamics of Matter, Hamburg, Germany. [4]Department of Physical Electronics, Tel Aviv University, Tel Aviv, Israel. [5]Chemistry Department, Tel Aviv University, Tel Aviv, Israel. [6]Raymond and Beverly Sackler Faculty of Exact Science, School of Chemistry and Center for Light-Matter Interaction, Tel Aviv University, 6997801 Tel-Aviv, Israel.
*Corresponding author. Email: gavrielerner@gmail.com (G.L.); oren@technion.ac.il (O.C.)

be repeated until it returns to the identity, i.e., it the first integer for which $\hat{G}^n = 1$.

The field $\vec{E}$ can exhibit a large variety of symmetries depending on the role played by its microscopic and macroscopic DOF. First, the polarization components could have intricate dependencies among themselves along the time axis, resulting in microscopic symmetries. These DSs have recently been fully described by a local Floquet group theory (*13*), where general DSs involve products of temporal operations (either time translations by time T/n, where T is the temporal period, denoted by $\hat{\tau}_n$ or time reversal denoted by $\hat{T}$; see table S1) and local spatial operations (summarized in table S2) that intermix the polarization components and are equivalent to point group symmetries (local rotations by $2\pi m/n$ around axis j, denoted by $\hat{r}^j_{n,m}$; local reflections, denoted by $\hat{\sigma}$; local inversion, denoted by $\hat{i}$; and local improper rotations by $2\pi m/n$, denoted by $\hat{s}_{n,m}$). Second, the field could have symmetries associated with its macroscopic structure and spatial dependence as well as its temporal behavior (*20*). In this case, the spatial symmetry operations comprise the space group symmetries that include point group operators denoted by capital letters (these are not to be confused with the lowercase letter operators, which act on the local field polarization components). Besides point group operations, spatial translations are also possible (where translation by Lm/n along the j axis is denoted by $\hat{J}_{n,m}$, and L is the minimal spatial period along the jth axis). Last, a periodic space-time (but aperiodic in time or space) field is invariant under a mixed operation of macro–space-time translations, $\hat{D}_n$. We emphasize that the operations acting on the microscopic and macroscopic scales need not be the same ones. Together, these options give rise to a rich and diverse theory that describes the symmetries of $\vec{E}$, with $(N + M + 1)$ DOF, where N is the number of local DOF, M is the number of macroscopic DOF, and "1" is the time dimension. The recent local Floquet group theory spans the (3 + 0 + 1) case (*13*, *22*), while the group theory for time-dependent crystals is described by the (0 + 3 + 1) case (*20*). For ordered nonperiodic systems, e.g., quasicrystals (*23*) and optical quasicrystals (*24*, *25*), we use superspace concepts (*21*), where M is larger than the physical macroscopic dimension (see the "Space-time polarized quasicrystal" section).

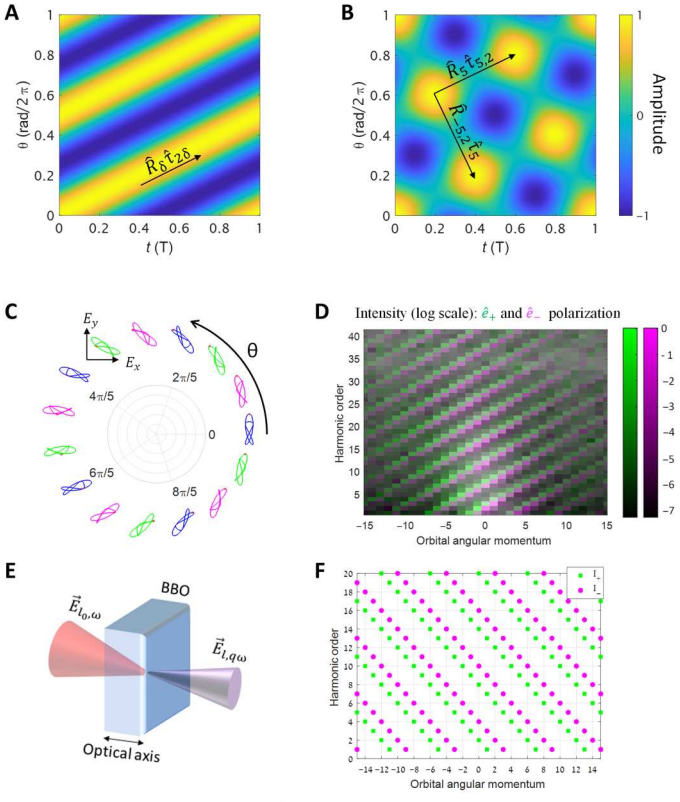

Fig. 1. Examples of symmetries and selection rules of EM waves with angular momentum. (**A**) A monochromatic field with OAM $[\vec{E}(\theta, t) \propto \cos(\omega t - 2\theta)]$ with a continuous symmetry of macroscopic rotation and time translation, $\vec{E}(\theta, t) = \vec{E}(\theta + \delta, t + 2\delta/\omega)$, i.e., $\hat{R}_\delta \hat{\tau}_{2\delta}$. (**B**) The superposition of two fields, cos(ωt + 2θ) + cos (2ωt − θ), has the fifth-order discrete symmetries, $\hat{R}_{4,-1}\hat{\tau}_{4,1}$ and $\hat{i}\hat{R}_{4,1}\hat{\tau}_{4,1}$. (**C**) The superposition of three circularly polarized fields, $\hat{e}_+\cos(2\omega t - \theta) + \hat{e}_-[\cos(2\omega t) + \cos(3\omega t + \theta)]$, exhibits the multiscale DS, $\hat{R}_{5,-1}\hat{\tau}_{5,1}\hat{r}_{5,2}$. The Lissajous curve of the local field is plotted every 2π/15 rotation of θ. The shape of the Lissajous curve repeats itself every 2π/5 rotation in θ followed with rotation of the polarization by −4π/5 and −*T*/5 time translation, which is indicated by a red dot at $t = 0$. However, there is no symmetry between the local fields at arbitrary angles, as can be seen in the nonidentical Lissajous curves for fields that are separated by 2π/15. (**D**) The simulated intensity of the harmonics emitted from the field in (C) clearly demonstrates the selection rule $q - l \pm 2 = 5Q$ for left $(\hat{e}_+)$ and right $(\hat{e}_-)$ circularly polarized harmonics. (**E**) Circularly polarized field with orbital momentum, $\vec{E} \propto \hat{e}_+ \exp[i(\omega t + l_0\theta)]$, propagating along the optical axis of a β-BaB2O4 (BBO) crystal generating harmonic field. (**F**) The selection rules for the harmonic order OAM and helicity of the generated harmonics in the BBO crystal.

We can systematically formulate all the possible DSs that $\vec{E}$ may exhibit by considering all possible products of the above building block operators (on both scales). This combinatorial large ensemble of options can be slightly reduced in size by considering the following: (i) For the group to exhibit closure, a DS can only combine different operations of a commensurate order (*13*), and (ii) we are only interested in the unexplored types of DSs that involve operations on the macroscopic scale (as the microscopic theory is already well-established). With this in mind, we begin mapping out DSs according to their dimensionality and whether they involve different length scales. For instance, we define a general operation that involves both a temporal operator (e.g., time translation or reversal) and a macroscopic operation (e.g., rotation or reflection), hence denoted as macro–space-time operation, $\hat{M}$, by

$$\hat{M}\vec{E}(\vec{R}, t) = \vec{E}(\hat{\Gamma}_R\vec{R} + \vec{u}, st + \tau) = \vec{E}(\hat{\Gamma}\vec{X} + \vec{a}) \qquad (2)$$

where $\hat{\Gamma}_R$ is an M-dimensional point group operation, $s = \pm 1$ indicates the possible action of time reversal, and $(\vec{u}, \tau) \equiv \vec{a}$ is a vector that denotes translations in space and time, respectively. Table S1 summarizes the macro–space-time operation building blocks, which construct the general operator $(\hat{M})$. We note that the order of the composite operation is the lowest common multiple of the order of the building block operators.

It is instructive to consider a concrete physical example of an EM field that exhibits such a macro–space-time symmetry. For instance, an EM field with temporal frequency ω, carrying orbital angular momentum (OAM), which is characterized by the phase winding number (or topological charge) l, has a continuous symmetry of macroscopic rotation with time translation:

$\vec{E}(\theta,t) = \vec{E}(\theta+\delta, t+l\delta/\omega)$, i.e., it is invariant under $\hat{M} = \hat{R}_\delta \hat{\tau}_{l\delta}$ (Fig. 1A), where δ is any real number, and $\hat{R}_\delta$ is a rotation of δ angle and $\hat{\tau}_{l\delta}$ is translation by $l\delta$ (we use this kind of notation for continuous DS). Figure 1B shows another example of the macro–space-time symmetry of a superposition of two fields $\cos(\omega t + 2\theta) + \cos(2\omega t - \theta) l_1 = 1$ and $l_2 = -1$, which exhibit the symmetry $\vec{E}(\theta,t) = \vec{E}(\theta + 2\pi/5, t + 2T/5)$, i.e., $\hat{M} = \hat{R}_5 \hat{\tau}_{5,2}$. That is, the overall EM field is invariant under the combined operations of a rotation by $-2\pi/4$ in θ and a time translation by $T/4$.

Next, we explore multiscale DSs (i.e., products of both microscopic and macroscopic operations, which are typically different from each other). These operations take on the form

$$\hat{\gamma}\hat{M}\vec{E} = \hat{\gamma}\vec{E}(\hat{\Gamma}\vec{X} + \vec{a}) \tag{3}$$

where $\hat{\gamma}$ is a point group microscopic operation that acts on the polarization DOF of $\vec{E}$. For a general vector field, $\hat{\gamma}$ can act on all local parameters such as spin (*26*) and color (*27*, *28*). Table S2 summarizes all the building blocks for microscopic operation. As an example, Fig. 1C shows a superposition of three twisted EM beams with circular polarization that exhibits the high-order multiscale DS, $\hat{R}_{5,-1}\hat{\tau}_{5,1}\hat{r}_{5,2}$. That is, the overall EM field in Fig. 1C is invariant under the following combined operations: a rotation by $-2\pi/5$ in θ, a time translation by $T/5$, and a rotation of the polarization by $4\pi/5$. This is an example of a DS that combines macroscopic and microscopic operations; however, the field itself is not invariant under pure microscopic or macroscopic operations, but only under the combined multiscale DS. The theory thus describes the physical manifestation of coupling between the different DOF of the EM field.

EM fields usually exhibit many DSs. For instance, the field in Fig. 1B has both $\hat{R}_{4,-1}\hat{\tau}_{4,1}$ and $i\hat{R}_{4,1}\hat{\tau}_{4,1}$ DSs, along with their various products and powers. The combination of DSs is best described by a group theory, where each group is closed and formed by a finite set of generating DSs. With this approach, the complete EM field can be obtained from the field information within a single unit cell and the comprising symmetry group (similar to solid-state lattices).

DSs of the induced polarization

Having discussed in general the DSs that characterize EM fields, we go on to apply the symmetry theory to light-matter interactions, focusing on the example of HHG. We consider the nonlinear interaction of a macroscopic medium irradiated by an electric field. Within the Born-Oppenheimer and dipole approximations, the microscopic Hamiltonian of a nonlinear system (in both the perturbative and non-perturbative regimes) at a macroscopic point, $\vec{R}$, interacting with a laser field that is given in atomic units and in the length gauge, is given by

$$\hat{H}_{\vec{R}}(t) = \sum_j -\frac{\nabla_j^2}{2} + \frac{1}{2}\sum_{i\neq j}|\vec{r}_i - \vec{r}_j|^{-1} + \sum_j U_{\vec{R}}(\vec{r}_j) + \sum_j \vec{E}(\vec{R},t)\cdot\vec{r}_j \tag{4}$$

where $\vec{r}_j$ is the microscopic coordinate of the jth electron, and $U_{\vec{R}}$ is the time-independent potential that is associated with the electrostatic interactions of electrons in the system with the nuclei. We assume here that the long-range interactions between the different macroscopic points is negligible; therefore, the full wave function of the noninteracting microscopic systems is a noninteracting product of the microscopic wave functions in different spatial positions: $|\psi(t)\rangle = \prod_{\vec{R}} |\psi_{\vec{R}}(t)\rangle$, where $|\psi_{\vec{R}}(t)\rangle$ is the wave function of a microscopic system located at $\vec{R}$. Even if the microscopic Hamiltonian and wave function lack any microscopic DS, the total Hamiltonian that the same amplitude includes the macroscopic structure, $\hat{H}(t) = \sum_{\vec{R}} \hat{H}_{\vec{R}}(t)$, and the full wave function can exhibit multiscale DSs. This can happen if all of the following exhibit a shared multiscale DS: (i) the electric field $\vec{E}(\vec{R},t)$, (ii) the sum of the microscopic potentials $U = \sum_{\vec{R}} U_{\vec{R}}$, and (iii) the wave function of the initial state [which is typically the ground state of $\hat{H}(t)$ with $\vec{E}(\vec{R},t) = 0$] (for proof, see section S1). When $|\psi(t)\rangle$ exhibits a DS, the observables also uphold symmetry relations; the induced polarization $\vec{P}(\vec{R},t)$ that is odd under parity also upholds the same DS (see section S1). Notably, while here we explore selection rules in systems with multiscale DSs within the dipole approximation, the approach can, in principle, be applied to systems where nondipole effects are substantial. In these cases, one could treat the entire macroscopic system with a single parameter r or have terms in the Hamiltonian that couple between the microscopic and macroscopic coordinates. In both cases, one would need to identify the DSs of the Hamiltonian.

Constraints on the Fourier spectrum of the induced polarization

To analytically derive the selection rules due to DSs exhibited by $\hat{H}(t)$, we analyze a general $\vec{P}(\vec{R},t)$ function in the Fourier domain

$$\vec{P}(\vec{R},t) = \vec{P}(\vec{X}) = \sum\nolimits_{\vec{k}} \vec{F}(\vec{k})\exp(i\vec{k}\cdot\vec{X}) \tag{5}$$

When $\vec{P}(\vec{X})$ is invariant under a general multiscale DS

$$\vec{P}(\vec{X}) = \hat{G}^{-1}\vec{P}(\vec{X}) = \hat{\gamma}^{-1}\vec{P}(\hat{M}\vec{X}) = \hat{\gamma}^{-1}\vec{P}(\hat{\Gamma}^{-1}\vec{X} - \vec{a}) \tag{6}$$

its Fourier decomposition must fulfill (for full derivation see section S3)

$$\hat{\gamma}\vec{F}(\hat{\Gamma}\vec{k})\exp(i\vec{k}\cdot\vec{a}) = \vec{F}(\vec{k}) \tag{7}$$

Equation 7 implies that $\vec{F}(\vec{k})$ is nonzero only for certain values of $\vec{k}$ and for specific polarizations of $\vec{F}(\vec{k})$, i.e., the symmetry manifests in the spectral content of $\vec{F}(\vec{k})$. Also note that the same $\hat{\Gamma}$ appears in both real and Fourier domains. According to Eq. 7, spectral DOFs that do not appear in the DSs of the system are not restricted by the DS. Because $\vec{F}(\vec{k})$ denotes the Fourier decomposition of $\vec{P}(\vec{X})$, any DS exhibited by $\vec{P}(\vec{X})$ directly corresponds to restrictions, i.e., selection rules, on the spectral behavior of $\vec{F}(\vec{k})$. The three different kinds of possible restrictions are (i) forbidden harmonics, (ii) forbidden polarization of some harmonics, and (iii) harmonics that must have the same amplitude or polarization up to reflection or rotations. "Harmonics" in the context of selection rules denotes both the temporal and spatial frequency content of the emitted light, that is, selection rules can, and often do, lead to mixed restrictions that couple the spatial frequencies and

angular momenta with the temporal frequency and polarization components. In that sense, the multiscale theory leads to new types of generalized restrictions linking all DOFs of the emitted light. By definition, the Fourier coefficients $\vec{F}(\vec{k})$ are N-dimensional complex-valued vectors. To better understand the constraint of Eq. 7 on $\vec{F}(\vec{k})$, it is useful to express $\vec{F}(\vec{k})$ as the superposition $\vec{F}(\vec{k}) = \sum_{i=1}^{N} \exp[i\phi_i(\vec{k})] A_i(\vec{k}) \hat{F}_i(\vec{k})$, where the polarization components $[\hat{F}_i(\vec{k})]_i$ are orthogonal unit vectors (e.g., right- and left-handed circular unit vectors), $[A_i(\vec{k})]_i$ are their real positive amplitudes, and $[\phi_i(\vec{k})]_i$ are their phases. Such a decomposition is possible also for singular fields (*29*, *30*).

Consequently, Eq. 7 can be written as

$$\sum_i \exp[i\phi_i(\hat{\Gamma}\vec{k}) + i\vec{k}\cdot\vec{a}] A_i(\hat{\Gamma}\vec{k}) \hat{\gamma} \hat{F}_i(\hat{\Gamma}\vec{k}) = \sum_i \exp[i\phi_i(\vec{k})] A_i(\vec{k}) \hat{F}_i(\vec{k}) \quad (8)$$

which can have a nontrivial solution (i.e., at least one nonzero A_i) if the polarization of the $\hat{\Gamma}\vec{k}$ th harmonic under a $\hat{\gamma}$ microscopic operation is equal to the polarization of the $\vec{k}$ th harmonic up to some phase α_i: $\hat{\gamma}\sum_i A_i(\hat{\Gamma}\vec{k})\hat{F}_i(\hat{\Gamma}\vec{k}) = \exp(i\alpha_i)\sum_i A_i(\vec{k})\hat{F}_i(\vec{k})$. Overall, A_i can be nonzero only when the microscopic operation $\hat{\gamma}$ can be described as a product of two other microscopic operations, $\hat{\gamma}'$ and $\hat{\gamma}''$, which fulfill the following conditions: (i) $\hat{F}_i(\vec{k})$ and $\exp(i\alpha_i)$ are the ith eigenvector and eigenvalue of $\hat{\gamma}'$, respectively (table S2 lists possible eigenvectors and eigenvalues). $\hat{\gamma}''$ permutes the i indices of the polarizations, namely, (ii) $\hat{\gamma}''\hat{F}_i(\hat{\Gamma}\vec{k}) = \hat{F}_{i'}(\vec{k})$ and (iii) $A_i(\hat{\Gamma}\vec{k}) = A_{i'}(\vec{k})$. Besides these, another requirement for obtaining nontrivial and physically meaningful solutions is that the phase difference $\phi_i(\vec{k}) - \phi_{i'}(\hat{\Gamma}\vec{k})$ should uphold the equation

$$\phi_i(\vec{k}) - \phi_{i'}(\hat{\Gamma}\vec{k}) = \vec{k}\cdot\vec{a} + \alpha_i - 2\pi Q \quad (9)$$

where Q is any integer.

Selection rules

Equation 9, specifically, has different kinds of solutions depending on $\hat{\Gamma}$. For instance, if $\hat{\Gamma}$ is the identity operator, then the selection rule has the form $\vec{k}\cdot\vec{a} + \alpha_i = 2\pi Q$. This form appears in the selection rules in rows 4 to 8 in Table 1. This type of solution describes the allowed harmonics and their polarization in a similar manner to that of microscopic HHG. Alternatively, when the DS also involves macroscopic rotations ($\hat{\Gamma} = \hat{R}_{n,m}$), the equation for the phase of $\vec{F}(\vec{k})$ becomes $\phi(\hat{R}_{n,m}\vec{k}) = \phi(\vec{k}) + 2\pi lm/n$. Then, Eq. 9 leads to the condition $\vec{k}\cdot\vec{a} + 2\pi lm/n + \alpha_i = 2\pi Q$. Here, l is the allowed winding number that characterizes the OAM of the emitted $\vec{k}$ harmonic. Thus, assuming paraxiality of the emitted harmonic beam, the selection rules in this case describe the allowed harmonic indices, their OAMs, and their polarization states. When the DS involves macroscopic reflections or time reversal (e.g., $\hat{\Sigma}_x$ or $\hat{T}$), this restricts a pair of harmonics, e.g., $\vec{k}$ and $\hat{\Sigma}_x\vec{k}$, to have to same amplitude. The relationship between the polarization of each harmonic in the pair then depends on the microscopic operation $\hat{\gamma}$. When $\hat{\gamma}$ is the identity operator or a rotation, the pairs of harmonics have identical polarizations. When $\hat{\gamma}$ is either an improper rotation or a reflection, the polarizations of the harmonic pair are reflections of each other. In the most general case, all these different DOFs may be coupled in the sense that a given emitted harmonic order may only be emitted when its polarization state, its OAM, and its momentum all comply to a complex algebraic relationship. In section S4, we derive the selection rules for symmetries that include time reversal or space reflection [for the case of $(1 + 1 + 2)D$; rows 9 to 14 in Table 1].

So far, we have discussed discrete symmetries that are combinations of discrete operations. However, $\hat{G}$ can also be a continuous operator. For example, the continuous DSs $\hat{r}_{\delta\alpha}\vec{E}(\hat{R}_{\delta 2\pi m/n}\vec{X} + \delta\vec{a})$ for any real δ leads, according to Eq. 9, to the selection rules

$$\vec{k}\cdot\vec{a} + 2\pi lm/n \pm \alpha = 0 \quad (10)$$

which means that the combination of polarization, energy, and linear and angular momenta is constant and can be considered a conserved charge, in a similar manner to the conservation of torus knot angular momentum described in (*18*, *19*).

Notably, the derived selection rules determine which emission channels are allowed/forbidden by considering the symmetry of the system only. The theory is insensitive to the detailed dynamics of the system (e.g., electronic trajectories in HHG), which, if leads to allowed channels, will also determine their complex amplitudes.

Table 1 summarizes the different DSs in the $(2 + 1 + 1)D$ case (i.e., where there are two microscopic polarization dimensions, one time axis and one macroscopic axis) and their associated selection rules. We again emphasize that these involve new selection rules as compared to the microscopic theory (*13*), i.e., the inclusion of macroscopic DOF in the EM field can change the system's response and lead to new control mechanisms for XUV light in HHG or new routes for ultrafast spectroscopy. Higher dimensionalities can be similarly derived.

DSs and selection rules of twisted light

We demonstrate numerically that these analytically derived selection rules are upheld by using the Lewenstein model (due to its high numerical efficiency) (*32*) to calculate the HHG spectrum driven by the field $\vec{E}(\vec{R}, t)$. An example is shown in Fig. 1, $\vec{E}(\theta, t) \propto \hat{e}_+\cos(2\omega t - \theta) + \hat{e}_-[\cos(2\omega t) + \cos(3\omega t + \theta)]$, where $\hat{e}_+$ and $\hat{e}_-$ are the left- and right-rotating circularly polarized polarizations, respectively. This field exhibits a DS of $\hat{\tau}_{5,1}\hat{R}_{5,-1}\hat{r}_{5,2}$, and therefore, the selection rule for the harmonics emitted from this field (derived in Table 1, row 7) is $q - l \pm 2 = 5n$. Here, q is the temporal harmonic, l is the OAM winding number, and n is an integer, such that this selection rule essentially couples the harmonic order with its angular momenta and polarization in one generalized constraint, i.e., certain harmonic orders can only be emitted with certain values of OAM with (±) circular polarization. This type of coupling is not possible without the multiscale operations. The selection rule is numerically investigated in Fig. 1D, which shows the intensity of the left- and right-rotating harmonics as a function of q and l, agreeing well with the analytic theory.

Table 1. DSs and their associated selection rules in the (2 + 1 + 1)*D* case (i.e., where there are two microscopic polarization dimensions, one time axis, and one macroscopic axis). The harmonic order of the temporal (spatial) frequency is q_1 (q_2). Notably, the selection rules are affected by the inclusion of macroscopic operations. In row 1, a continuous space-time translation DS leads to energy-momentum conservation (*15*, *31*). In row 2, a continuous space-time translation and microscopic rotation DS leads to energy-momentum-spin conservation (*14*, *16*, *18*). In row 3, the DS is the same as in row 2, except that here the rotation is along an ellipse in which the ratio of the minor to major axis is *b*. This leads to energy-momentum-ellipticity conservation.

	Dynamical symmetry	Spectral selection rule	Polarization
1	$\hat{\tau}_\delta \hat{J}_{\beta\delta}$	$q_1 + \beta q_2 = 0$	Any
2	$\hat{\tau}_\delta \hat{J}_{\beta\delta} \hat{r}_{\alpha\delta}$	$q_1 + \beta q_2 \pm \alpha = 0$	(±) Circular
3	$\hat{\tau}_\delta \hat{J}_{\beta\delta} \hat{e}_{\alpha\delta}$	$q_1 + \beta q_2 \pm \alpha = 0$	Ellipticity of ±*b*
4	$\hat{\tau}_2 \hat{J}_2, \hat{\tau}_2 \hat{J}_2 \hat{r}_2$	$q_1 + q_2 =$ odd	Any
5	$\hat{\tau}_2 \hat{J}_2 \hat{\sigma}$	$q_1 + q_2 =$ even	In $\hat{\sigma}$ plane
		$q_1 + q_2 =$ odd	Orthogonal to $\hat{\sigma}$ plane
6	$\hat{\tau}_{n_0} \hat{J}_{n_0,m}$	$q_1 + q_2 = n_0 n$	Any
7	$\hat{\tau}_{n_0,m_1} \hat{J}_{n_0,m_2} \hat{r}_{n_0,m_3}$	$q_1 m_1 + q_2 m_2 \pm m_3 = n_0 n$	(±) Circular
8	$\hat{\tau}_{n_0,m_1} \hat{J}_{n_0,m_2} \hat{e}_{n_0,m_3}$	$q_1 m_1 + q_2 m_2 \pm m_3 = n_0 n$	Ellipticity of ±*b*
9	$\hat{I}, \hat{I}\hat{r}_2, \hat{I}\hat{\tau}_2 \hat{J}_2 \hat{r}_2$	$A_{q_1,q_2} = A_{-q_1,-q_2}$	Linear, $\hat{F}_{q_1,q_2} = \hat{F}_{-q_1,-q_2}$
10	$\hat{I}\hat{\sigma}, \hat{I}\hat{\tau}_2 \hat{J}_2 \hat{\sigma}$	$A_{q_1,q_2} = A_{-q_1,-q_2}$	Ellipse axis orthogonal to $\hat{\sigma}$ plane, $\hat{F}_{q_1,q_2} = \hat{\sigma}\hat{F}_{-q_1,-q_2}$
11	$\hat{\Sigma}_x \hat{\tau}_2, \hat{\Sigma}_x \hat{\tau}_2 \hat{r}_2$	$A_{q_1,q_2} = A_{q_1,-q_2}$	$\hat{F}_{q_1,q_2} = \hat{F}_{q_1,-q_2}$
12	$\hat{\Sigma}_x \hat{\tau}_2 \hat{\sigma}$	$A_{q_1,q_2} = A_{q_1,-q_2}$	$\hat{F}_{q_1,q_2} = \hat{\sigma}\hat{F}_{q_1,-q_2}$
13	$\hat{T}\hat{J}_2, \hat{T}\hat{J}_2 \hat{r}_2$	$A_{q_1,q_2} = A_{-q_1,q_2}$	Linear
14	$\hat{T}\hat{J}_2 \hat{\sigma}$	$A_{q_1,q_2} = A_{-q_1,q_2}$	Ellipse axis orthogonal to $\hat{\sigma}$ plane

Our theory is also applicable to non-isotropic and inhomogeneous media. All that is needed is to address the symmetry of the light-matter system that has the shared symmetry of the light part and the matter part, which will have lower symmetry in case of non-isotropic and inhomogeneous media. For example, following a recent publication (*33*), we investigate the symmetries and selection rules of a circularly polarized field with orbital momentum, $\vec{E} \propto \hat{e}_+ \exp[i(\omega t + l_0\theta)]$, propagating along the optical axis of a β-BaB_2O_4 (BBO) crystal (Fig. 1E). Tang *et al.* (*33*) explored experimentally the emitted second harmonic generation (SHG) in this system, with $l_0 = 0$ or 1, and observed that SHG fields of the forms $\hat{e}_- \exp[i(2\omega t + 2l_0\theta)]$, $\hat{e}_+ \exp\{i[2\omega t + (2l_0 - 2)\theta]\}$, and $\hat{e}_+ \exp\{i[2\omega t + (2l_0 + 4)\theta]\}$ were generated. These results were explained by a cascaded linear spin-orbit interaction and a perturbative nonlinear interaction. As shown below, our theory (which is valid in the perturbative and nonperturbative regimes) directly yields all of the allowed channels, only some of which were obtained by the cascaded model (*33*).

The BBO crystal irradiated by the field $E \propto \hat{e}_+ \exp[i(\omega t + l_0\theta)]$ has the combined symmetry of $\hat{\tau}_{6,l_0+4}\hat{R}_{6,-1}\hat{r}_{6,2}$. Therefore, according to Eq. 9, the selection rules are $q(l_0 + 4) - l + 2s = 6Q$, where q is the temporal harmonic, l is the OAM winding number, s is the spin, and Q is an integer. Hence, for SHG ($q = 2$), we get the selection rule for the OAM with spin, $s = \pm 1$

$$l = 6Q + 2 + 2l_0 \pm 2 \tag{11}$$

This result agrees with the measured and predicted results in (*33*) and also predicts more allowed channels (see Fig. 1F showing the rich structure of the various allowed channels).

Space-time polarized quasicrystal

We now apply the theory to nonperiodic systems, e.g., quasicrystals (*23*) and optical quasicrystals (*24*, *25*), by using the superspace concept (*21*), where M (the effective number of macroscopic DOF) is larger than the physical macroscopic dimension. We demonstrate this option by deriving the HHG selection rules driven by a field with a spatiotemporal quasi-periodic structure. Specifically, we consider a superposition of four fields that interact with an isotropic argon gas medium with thickness much smaller than the coherent length. The vectorial time-space quasicrystal arises from the structure of the electric field, not from the medium. The field, limited to the (t, X) axes [i.e., dimensionality of $(2 + 1 + 1)D$], is described by

$$\begin{aligned}\vec{E}(t, X) = A\{&\cos[\omega t + (1 + \sqrt{2})kX] - \cos[(1 + \sqrt{2})\omega t - kX]\}\hat{x} \\ &+ \{\cos[(1 + \sqrt{2})\omega t + kX] - \cos[\omega t - (1 + \sqrt{2})kX]\}\hat{y}\end{aligned} \tag{12}$$

This field has a vectorial quasicrystal structure in space-time, as shown in Fig. 2A. Using the superspace representation [with dimensionality $(2 + 4 + 4)D$], the field can be rewritten in superspace as

$$\begin{aligned}&\vec{E}(t_1, t_2, t_3, t_4, X_1, X_2, X_3, X_4) \\ &= A\{\cos[\omega t_1 + (1 + \sqrt{2})kX_1] - \cos[(1 + \sqrt{2})\omega t_2 - kX_2]\}\hat{x} \\ &+ \{\cos[(1 + \sqrt{2})\omega t_3 + kX_3] - \cos[\omega t_4 - (1 + \sqrt{2})kX_4]\}\hat{y}\end{aligned} \tag{13}$$

where X_j are new coordinates introduced in the higher dimensionality of the superspace representation. In this picture, $\vec{E}$ is periodic in all coordinates $X_{j=1,2,3,4}$. Therefore, the induced polarization will also be periodic in $X_{j=1,2,3,4}$. The induced polarization can then be expressed with spatial frequencies of $\vec{k} = \sum_{j=1}^{4} q_j \vec{b}_j = q_1(1 + \sqrt{2})k\hat{X}_1 - q_2 k\hat{X}_2 + q_3 k\hat{X}_3 - q_4(1 + \sqrt{2})k\hat{X}_4$, where q_j is an integer, which also corresponds to the number of photons annihilated from each field.

To obtain the HHG selection rules, we project the superspace representation back to physical space, i.e., take $\hat{X}_1 = \hat{X}_2 = \hat{X}_3 = \hat{X}_4 \to \hat{X}$. Following this, the allowed X axis spatial frequencies are $k_{\vec{q}}^{(X)} = q_1(1 + \sqrt{2})k - q_2 k + q_3 k - q_4(1 + \sqrt{2})k$, which is equivalent to a condition of conservation of X axis momentum. Other symmetries also connect the spatial and temporal harmonic orders. For instance, the continuous symmetry $\vec{E}\left[t_1 + \frac{\delta}{\omega}, t_2, t_3, t_4, X_1 - \delta/(1 + \sqrt{2})k, X_2, X_3, X_4\right] = \vec{E}(\vec{t}, X_1, X_2, X_3, X_4)$ for any δ, which is associated with the

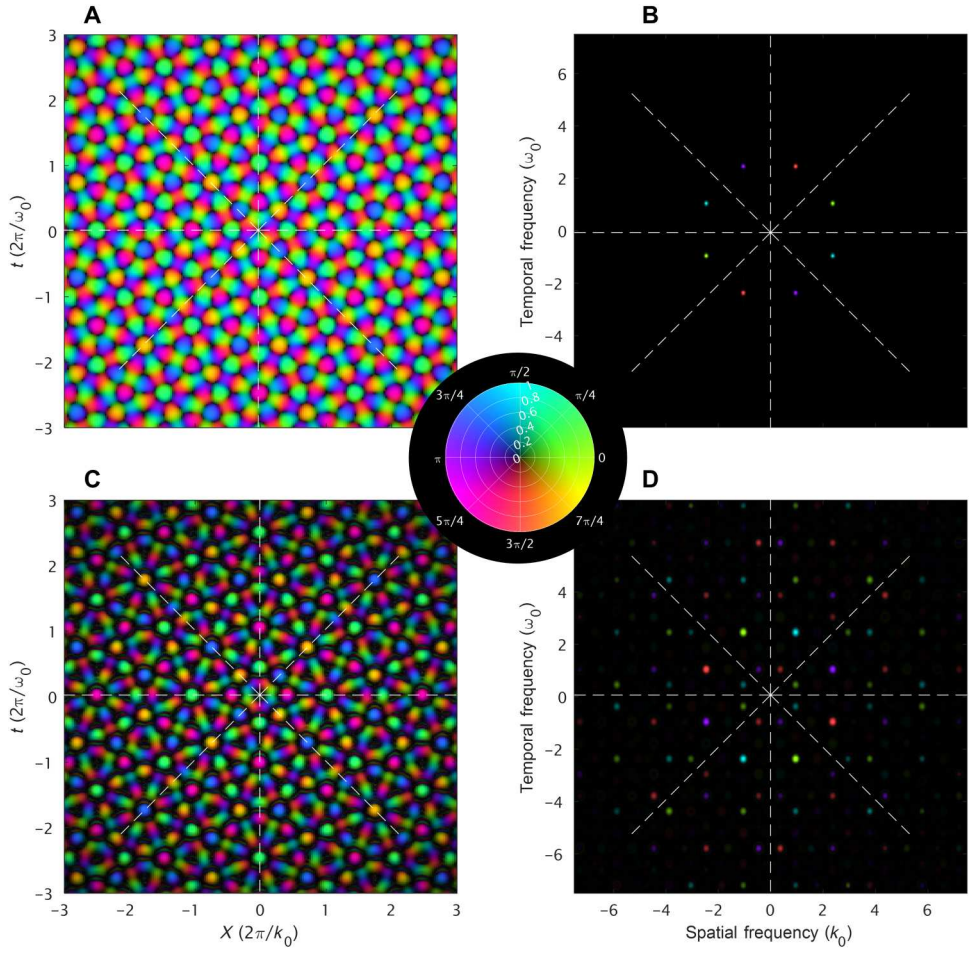

Fig. 2. Nonlinear wave mixing in optical time-space vectorial quasicrystal. (**A**) The electric field in normalized space and time poses an octagonal quasicrystal vectorial structure. The direction and amplitude of the polarization is mapped to a color according to the center plot. (**B**) The Fourier representation of the octagonal quasicrystal field has a simpler octagonal structure with eight peaks, where the polarization from one peak to the other is rotated by π/2. (**C**) The complex quasicrystal symmetry is conserved in the simulated induced polarization, $\overrightarrow{P}$. (**D**) More peaks, i.e., more harmonics, are generated in the induced polarization, and the polarized octagonal structure is conserved.

evolution of only the first subfield of the four subfields in Eq. 12. By applying Eq. 9, we arrive at the constraint $\overrightarrow{k}\cdot\overrightarrow{a}=q_1'-q_1=0$, where q_1 is the spatial $\hat{X}_1$ harmonic and q_1' is the temporal t_1 harmonic, $q_1'=q_1$. Similarly, this relationship is valid to all the subfields; hence, $q_j'=q_j$, indicating that the emitted $\omega_{\vec{q}}$ temporal harmonics have the same q_j of $k_{\vec{q}}^{(X)}$:$\omega_{\vec{q}}=q_1\omega+q_2(1+\sqrt{2})\omega+q_3(1+\sqrt{2})\omega+q_4\omega$. In the photonic picture, this means that each annihilated photon gives its energy and momentum to the generated $\omega_{\vec{q}}$ photon.

The field in Eq. 12 also exhibits the following two DSs: $\hat{\sigma}_x\overrightarrow{E}\left(t,X_1+\frac{\pi}{(1+\sqrt{2})k},X_2+\frac{\pi}{k},X_3,X_4\right)=\overrightarrow{E}(t,X_1,X_2,X_3,X_4)$ and $\hat{\sigma}_y\overrightarrow{E}\left(t,X_1,X_2,X_3+\frac{\pi}{k},X_4+\frac{\pi}{(1+\sqrt{2})k}\right)=\overrightarrow{E}(x,t_1,t_2,t_3,t_4)$. Applying our theory to these DSs (Eq. 7) yields

$$\begin{aligned}\hat{\sigma}_x\overrightarrow{F}(\overrightarrow{k})\exp[i(q_1+q_2)\pi]&=\overrightarrow{F}(\overrightarrow{k})\\ \hat{\sigma}_y\overrightarrow{F}(\overrightarrow{k})\exp[i(q_3+q_4)\pi]&=\overrightarrow{F}(\overrightarrow{k})\end{aligned}\tag{14}$$

Equation 14 dictates that harmonics with an odd q_1+q_2 and an even q_3+q_4 are x-polarized, harmonics with an even q_1+q_2 and an odd q_3+q_4 are y-polarized, and all other harmonics are forbidden. The field in Eq. 12 also exhibits higher symmetries because of its space-time polarized octagonal quasicrystal structure. The octagonal quasicrystal with an eightfold symmetry is well-known in crystallography of two-dimensional (2D) static spatial arrangements of atoms (*34*). Here, the vector electric field exhibits symmetries that are combinations of the d_8 dihedral group operations in space-time followed by microscopic operations

$$\begin{aligned}\hat{r}_4\overrightarrow{E}[\hat{R}_8(\zeta,\eta)]&=\hat{\sigma}_{\frac{3\pi}{4}}\overrightarrow{E}[\hat{\Sigma}_{0\text{ or }\frac{\pi}{2}}(\zeta,\eta)]=\hat{\sigma}_{\frac{\pi}{4}}\overrightarrow{E}[\hat{\Sigma}_{\frac{\pi}{4}\text{ or }\frac{3\pi}{4}}(\zeta,\eta)]\\&=\overrightarrow{E}[\hat{\Sigma}_{\frac{1+2n}{8}\pi}(\zeta,\eta)]=\overrightarrow{E}(\zeta,\eta)\end{aligned}\tag{15}$$

where the subscript of $\hat{\sigma}$ ($\hat{\Sigma}$) denote the angle of the reflection axis in the $x-y$ ($\zeta-\eta$) plane, and n is an integer, and where $\zeta=kx$ and $\eta=\omega t$ are the dimensionless space-time variables. According to Eq. 7, the polarized octagonal symmetries appear also in the Fourier domain of the driving field in Eq. 12. This field has eight

peaks in the Fourier domain (Fig. 2B), where each peak is linearly polarized along $\hat{x}$ or $\hat{y}$ rotated $\pi/2$ from the next peak, which is rotated by $\pi/4$ in the Fourier plane, as expected from Eq. 15. In addition, the induced polarization, calculated in argon by the Lewenstein model (*32*), exhibits symmetries in the space-time domain (Fig. 2C) and in the Fourier domain (Fig. 2D)

$$\hat{r}_4 \vec{F}(\hat{R}_8 \vec{\tilde{k}}) = \hat{\sigma}_{\frac{3\pi}{4}} \vec{F}(\hat{\Sigma}_{0 \text{ or } \frac{\pi}{2}} \vec{\tilde{k}}) = \hat{\sigma}_{\frac{\pi}{4}} \vec{F}(\hat{\Sigma}_{\frac{\pi}{4} \text{ or } \frac{3\pi}{4}} \vec{\tilde{k}}) = \vec{F}(\hat{\Sigma}_{\frac{1+2n}{8}\pi} \vec{\tilde{k}}) = \vec{F}(\vec{\tilde{k}}) \quad (16)$$

where $\vec{\tilde{k}}$ is a vector composed of the two dimensionless frequencies, ζ and η.

Experimental observation of multiscale DS and selection rules

We investigate experimentally an HHG selection rule that is based on a $(2 + 1 + 1)D$ multiscale DS, i.e., DS in two microscopic dimensions, time, and one macroscopic dimension, which is the propagation axis. The experimental laser field consists of three beams: a bicircular beam and additional Bessel beam, with the following form

$$\vec{E}_{\varphi}(t,z,\rho) = \hat{e}_+ e^{-(\rho/w)^2} a_1 \cos(\omega t') + \hat{e}_- e^{-(2\rho/w)^2} a_2 \cos(2\omega t') + \vec{E}^{\text{Bessel}}_{\varphi}(t,z,\rho) \quad (17)$$

where z is the propagation axis, ρ is the radial axis, t' is the retarded time ($t' = t - z/c$), w is the waist of the ω Gaussian beam, and a_1 and a_2 are the amplitudes of the beams. The Bessel beam is given by

$$\vec{E}^{\text{Bessel}}_{\varphi}(t,z,\rho) = a_3[\sin(\varphi + \pi/4)\hat{e}_+ + \sin(\varphi - \pi/4)\hat{e}_-]\cos(\omega t' + \beta z) J_0(\sqrt{2k\beta - \beta^2}\rho) \quad (18)$$

where a_3 is the amplitude, $k = \omega/c$ is the wave vector, β is the on-axis difference between the wave vectors of the Gauss and Bessel beams, J_0 is the zero-order Bessel function of the first kind, and ϕ controls the polarization of the Bessel beam. [In this experiment, ϕ corresponds to the angle between the optical axis of the quarter-wave plate (QWP) and the axis of the incoming linearly polarized Bessel beam.] The use of the Bessel beam allows us tunable control over the shape and structure of the light beam in mutliscale dimensionality—the polarization states of the beams control the microscopic dimensions, and the difference in phase velocity between the bicircular and Bessel beams allows to generate macroscopic structures along the z axis (the beams′ propagation axis) (*35*). Overall, these knobs allow us to tune the DSs of the field, including generation of multiscale symmetries, even when the system does not exhibit a unique symmetry in microscopic space alone. For example, when $\phi = \pi/4$, the polarization of $\vec{E}^{\text{Bessel}}$ is $\hat{e}_+$, similar to that of the ω Gaussian beam. Therefore, the total field exhibits the microscopic DS, $\hat{r}_{3,1} \vec{E}_{\varphi=\frac{\pi}{4}}(t - T/3, z, \rho) = \vec{E}_{\varphi=\frac{\pi}{4}}(t, z, \rho)$, i.e., the well-studied threefold microscopic rotational DS of the counter-rotating bicircular field that leads to the selection rule, $q = 3Q \pm 1$, with circular polarization, $\hat{e}_{\pm}$ (*36*). On the other hand, for $\phi = -\pi/4$ (and a polarization of $\vec{E}^{\text{Bessel}}_{\varphi=-\pi/4}$ that is $\hat{e}_-$, similar to the 2ω Gaussian beam), the total field does not exhibit any microscopic DS; rather, it only exhibits a multiscale DS that also involves translation operations along its propagation axis, $\hat{r}_{3,1} \vec{E}_{\varphi=-\frac{\pi}{4}}(t - T/3, z + L/3, \rho) = \vec{E}_{\varphi=-\frac{\pi}{4}}(t, z, \rho)$, where $L = 2\pi/\beta$ is the spatial period of the total field. According to Eq. 9, this multiscale DS should lead to the selection rule, $q_1 - q_2 = 3Q \pm 1$, with circular polarization $\hat{e}_{\pm}$, where q_1 and q_2 are the temporal and longitudinal harmonic orders, respectively. Last, when $\phi \neq \pi/4 + n\pi$, the total field lacks any DS, and therefore, all the harmonic orders and polarizations are allowed.

We shall now focus on the case when $\phi = -\pi/4$, which leads to multiscale DS. Figure 3A illustrates the $\hat{Z}_{3,1}\hat{\tau}_{3,-1}\hat{r}_{3,1}$ DS of the $\vec{E}_{\varphi=-\frac{\pi}{4}}$ field, where the time domain Lissajou curve is plotted every z step, visualizing a 3D surface (color-coding represents time). The three blue Lissajou plots are separated by $L/3$ from each other and show the multiscale $\hat{Z}_{3,1}\hat{\tau}_{3,-1}\hat{r}_{3,1}$ DS. Notably, this is a symmetry of all the electric fields involved in the light-matter interaction: each component of $\vec{E}$ and the XUV field (Fig. 3B). In the experiment, we only measured the XUV emission with small divergence, i.e., with $q_2 = 0$. This on-axis emitted XUV field is summed up coherently along the z axis during propagation (Fig. 3B). We first explore HHG in this scheme numerically. Figure 3C presents the microscopic yield of different harmonics as a function of ϕ. As shown, only $\phi = \pi/4$ (with the microscopic $\hat{\tau}_{3,-1}\hat{r}_{3,1}$ DS) leads to the forbidden $3Q$ harmonics. For $\phi = -\pi/4$, the yield of the $3Q$ harmonics is maximized. When we include propagation effects along the z axis (Fig. 3D), the $3Q$ harmonics become forbidden at $\phi = -\pi/4$ because of the multiscale $\hat{Z}_{3,1}\hat{\tau}_{3,-1}\hat{r}_{3,1}$ DS.

Our experimental setup is illustrated in Fig. 3E. The bicircular beam is formed by the MAZEL TOV apparatus (*37*). The Bessel beam is shaped by the spatial light modulator (SLM), and its polarization is controlled by the QWP angle, ϕ. Figure 3F shows the measured yield of harmonics 23 to 29 as a function of the QWP angle (each harmonic is normalized by its own peak intensity). The suppression of the $3Q$ harmonic orders for both the QWP angles at +45° and −45° (yielding $\phi = \pi/4$ and $\phi = -\pi/4$ in Eq. 18, respectively) is observed, as predicted from the selection rules by microscopic (+45°) and multiscale (−45°) DSs. The $3Q$ harmonics are not fully suppressed because of imperfect achromatic QWP in the MAZEL TOV apparatus, which leads to deviations from circular polarization in the bicircular field and by partial absorption of the harmonics in the interaction region as discussed in section S2.

DISCUSSION

We presented a theory for symmetries and selection rules in (extreme) nonlinear optics for multiscale systems. We introduced symmetries that couple time, macroscopic, and microscopic DOFs. We showed how these symmetries are transferred to the induced polarization and lead to constraints, i.e., selection rules, on physical observables. Multiscale DSs and selection rules investigations in three different systems are presented: with spin-orbit nonlinear interaction, with quasi-periodic structures, and experimental example with multiscale DS in time, polarization, and propagation axis.

A potential application of our theory is ultrafast spectroscopy for the detection of the symmetry of the medium. This is done using a

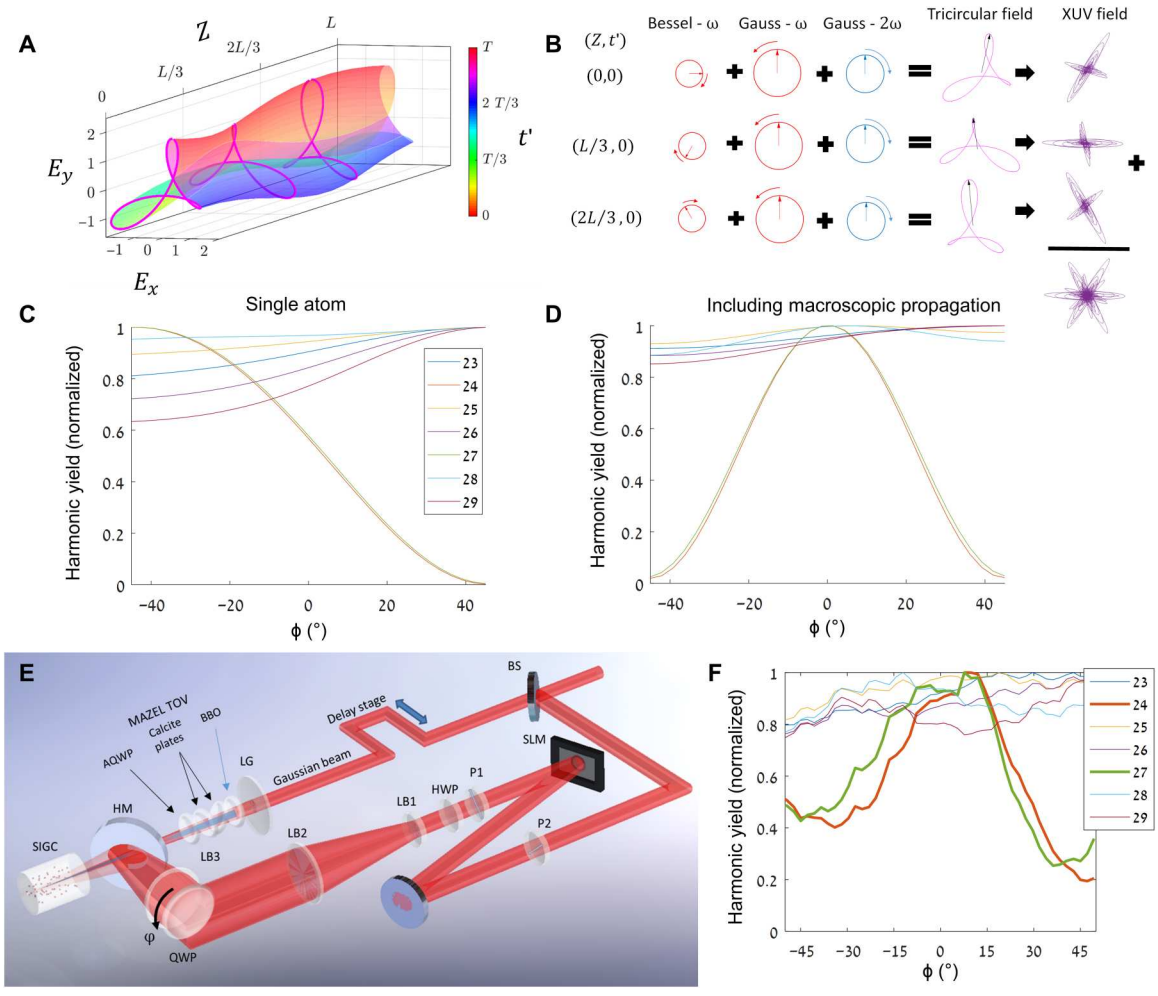

Fig. 3. Experimental investigation of selection rules in HHG due to multiscale dynamical symmetry. (**A**) The driver field (Eq. 17) with $\phi = -\pi/4$ plotted as a function of the propagation axis, Z, and retarded time, t' (shown in color). Plotting the fields during the three propagation steps shows a threefold $\hat{Z}_{3,1}\hat{\tau}_{3,1}\hat{r}_{3,-1}$ symmetry. (**B**) The output XUV field is a coherent sum of all the emitted XUV fields during propagation and has threefold $\hat{\tau}_{3,1}\hat{r}_{3,-1}$ symmetry, which results in the $3Q \pm 1$ selection rule. (**C**) Normalized intensity of several harmonic orders as a function of ϕ, calculated for only one propagation point, $\vec{E}_{\varphi}(t, z = 0, \rho)$. The $3Q$ harmonics are forbidden only when $\phi = 45°$. (**D**) Normalized intensity of several harmonic orders as a function of ϕ, calculated for $\vec{E}_{\varphi}(t, z, \rho)$. The $3Q$ harmonics (e.g., harmonics 24 and 27) are forbidden at both $\phi = -45°$ and $\phi = 45°$, which correspond to the $\hat{e}_-$ and $\hat{e}_+$ circular polarizations of the Bessel beam, respectively. The $3Q$ harmonics are forbidden at $\phi = 45°$ by the microscopic DS, $\hat{\tau}_{3,1}\hat{r}_{3,-1}$, and at $\phi = -45°$ by the multiscale DS, $\hat{Z}_{3,1}\hat{\tau}_{3,1}\hat{r}_{3,-1}$. (**E**) Schematic plot of the experimental setup. The driver field is prepared by focusing the bicircular $\omega - 2\omega$ Gaussian beams (produced by the MAZEL TOV apparatus) and the ω Bessel beam (shaped by the SLM) with controlled polarization (by the QWP) into the semi-infinite gas cell. (**F**) Normalized intensity of several harmonic orders as a function of the Bessel QWP angle, ϕ. Suppression of the $3Q$ harmonics (24,27) for both $-45°$ and $45°$ of the QWP, which leads to the $\hat{e}_-$ and $\hat{e}_+$ circular polarizations of the Bessel beam, respectively, are clearly observed. AQWP, achromatic QWP; SIGC, semi-infinite gas cell; SLM, spatial light modulator; LG, lens of Gaussian beam arm; LB, lens of Bessel beam arm; HM, holed mirror; BS, beam splitter; P, polarizer; HWP, half waveplate.

driving field that exhibits a known DS. When the medium lacks that DS, the symmetry of the total system is reduced so that some restrictions in the selection rules are removed (*38*). One important medium that breaks symmetries is a chiral medium, i.e., a medium that is asymmetric under any reflection or inversion. Probing the chirality of molecules can be a challenging task, and using multiscale DS consideration can help in choosing the right microscopic (*11*, *12*, *39*) and macroscopic field parameters to enhance the far-field chiral signal for molecular chirality detection and discrimination as shown in section S6. Our work also paves the way for several interesting directions beyond harmonic generation. Extending the theory to nonlocal interactions, which are especially important for HHG with long-wavelength high-power lasers (*40*) and condensed matter (*41*), may lead to insights regarding multiscale matter, light, and their interaction. Extensions to complexed structured laser ablation (*42*, *43*) or controlled optoelectronic (*44*) to easily shaping complex structures should also be possible and exciting, leading to inducing symmetries in the media. Overall, we expect that the use of multiscale symmetries will lead to extended understanding of, and novel findings in, various multiscale systems.

MATERIALS AND METHODS

The experimental setup is illustrated in Fig. 3E. The output beam of a 1-kHz, 35-fs full width at half maximum, 800-nm carrier wavelength, Ti:sapphire amplifier (Coherent Legend USX) is split into two paths. The first beam, with 2.25 mJ per pulse, retains its spatial Gaussian profile and is focused with a lens (f_{LG} = 300 mm, Rayleigh range of the Gaussian beams = 5 mm) through the MAZEL TOV apparatus (*37*). This apparatus consists of (i) an SHG crystal (0.5-mm-thick BBO crystal), which transfers ~15% of the energy to the second harmonic beam; (ii) calcite plates, which precompensate for group delays induced by normally dispersive optics down the beam path; and (iii) a single achromatic QWP (for the two spectral components) that converts the linear s-polarized fundamental and perpendicular p-polarized SH incoming beams to counter-rotating circularly polarized beams. This intense beam also drills a hole in the aluminum foil, terminating a semi-infinite gas cell (SIGC) filled with argon (45 torr). The second beam, with 0.5 mJ per pulse, undergoes an amplitude modulation using two perpendicularly oriented polarizers on either side of a phase-only SLM (HOLOEYE PLUTO). This beam acquires the spatial distribution of a ring, which is then imaged and focused (f_{LB3} = 150 mm) to form a Bessel beam with $\beta/k = 0.0015$. Here, $k = 2\pi/800$ nm is the wave vector, and β is the on-axis difference between the wave vectors of the Gauss and Bessel beams. This experimental condition corresponds to a periodicity of $L \approx 0.5$ mm, which is one order of magnitude smaller than the Rayleigh range. A QWP is used to scan the polarization of the Bessel beam. Both beams are combined using a holed mirror and are focused close to the output of the SIGC, where the high harmonic is generated. An aluminum filter downstream of the SIGS removes the pump beams before the spectrum of the HHG beam is measured using the XUV spectrometer. We first inserted only the bicircular Gaussian beam fields (i.e., without the Bessel beam) and phase-matched the HHG process by tuning the gas pressure, adjusting the location of the focus, and changing the opening of the aperture before the lens to maximize the $3n \pm 1$ harmonics. Then, we added the Bessel beam and measured the harmonic intensity generated by the total driver field as a function of the QWP angle (i.e., ϕ).

Supplementary Materials

This PDF file includes:

Sections S1 to S6
Fig. S1
Tables S1 and S2
References

REFERENCES AND NOTES

1. D. M. Bishop, *Group Theory and Chemistry* (Dover Publications, 1993).
2. C. L. Tang, H. Rabin, Selection rules for circularly polarized waves in nonlinear optics. *Phys. Rev. B* **3**, 4025–4034 (1971).
3. R. W. Boyd, *Nonlinear Optics*, vol. 5 of *Electronics & Electrical* (Academic Press, ed. 3, 2003).
4. O. E. Alon, V. Averbukh, N. Moiseyev, Selection rules for the high harmonic generation spectra. *Phys. Rev. Lett.* **80**, 3743–3746 (1998).
5. K. M. Dorney, L. Rego, N. J. Brooks, J. San Román, C.-T. Liao, J. L. Ellis, D. Zusin, C. Gentry, Q. L. Nguyen, J. M. Shaw, A. Picón, L. Plaja, H. C. Kapteyn, M. M. Murnane, C. Hernández-García, Controlling the polarization and vortex charge of attosecond high-harmonic beams via simultaneous spin–orbit momentum conservation. *Nat. Photonics* **13**, 123–130 (2019).
6. C. Hernández-García, A. Turpin, J. San Román, A. Picón, R. Drevinskas, A. Cerkauskaite, P. G. Kazansky, C. G. Durfee, Í. J. Sola, Extreme ultraviolet vector beams driven by infrared lasers. *Optica* **4**, 520 (2017).
7. F. Kong, C. Zhang, H. Larocque, Z. Li, F. Bouchard, D. H. Ko, G. G. Brown, A. Korobenko, T. J. Hammond, R. W. Boyd, E. Karimi, P. B. Corkum, Vectorizing the spatial structure of high-harmonic radiation from gas. *Nat. Commun.* **10**, 2020 (2019).
8. E. Frumker, N. Kajumba, J. B. Bertrand, H. J. Wörner, C. T. Hebeisen, P. Hockett, M. Spanner, S. Patchkovskii, G. G. Paulus, D. M. Villeneuve, A. Naumov, P. B. Corkum, Probing polar molecules with high harmonic spectroscopy. *Phys. Rev. Lett.* **109**, 233904 (2012).
9. D. Baykusheva, M. S. Ahsan, N. Lin, H. J. Wörner, Bicircular high-harmonic spectroscopy reveals dynamical symmetries of atoms and molecules. *Phys. Rev. Lett.* **116**, 123001 (2016).
10. S. Gholam-Mirzaei, J. Beetar, M. Chini, High harmonic generation in ZnO with a high-power mid-IR OPA. *Appl. Phys. Lett.* **110**, 061101 (2017).
11. O. Neufeld, D. Ayuso, P. Decleva, M. Y. Ivanov, O. Smirnova, O. Cohen, Ultrasensitive chiral spectroscopy by dynamical symmetry breaking in high harmonic generation. *Phys. Rev. X* **9**, 031002 (2019).
12. D. Ayuso, O. Neufeld, A. F. Ordonez, P. Decleva, G. Lerner, O. Cohen, M. Ivanov, O. Smirnova, Synthetic chiral light for efficient control of chiral light–matter interaction. *Nat. Photonics* **13**, 866–871 (2019).
13. O. Neufeld, D. Podolsky, O. Cohen, Floquet group theory and its application to selection rules in harmonic generation. *Nat. Commun.* **10**, 405 (2019).
14. O. Kfir, P. Grychtol, E. Turgut, R. Knut, D. Zusin, A. Fleischer, E. Bordo, T. Fan, D. Popmintchev, T. Popmintchev, H. Kapteyn, M. Murnane, O. Cohen, Helicity-selective phase-matching and quasi-phase matching of circularly polarized high-order harmonics: Towards chiral attosecond pulses. *J. Phys. B At. Mol. Opt. Phys.* **49**, 123501 (2016).
15. A. Bahabad, M. M. Murnane, H. C. Kapteyn, Quasi-phase-matching of momentum and energy in nonlinear optical processes. *Nat. Photonics* **4**, 571–575 (2010).
16. L. Z. Liu, K. O'Keeffe, S. M. Hooker, Optical rotation quasi-phase-matching for circularly polarized high harmonic generation. *Opt. Lett.* **37**, 2415–2417 (2012).
17. D. Azoury, O. Kneller, M. Krüger, B. D. Bruner, O. Cohen, Y. Mairesse, N. Dudovich, Interferometric attosecond lock-in measurement of extreme-ultraviolet circular dichroism. *Nat. Photonics* **13**, 198–204 (2019).
18. E. Pisanty, L. Rego, J. San Román, A. Picón, K. M. Dorney, H. C. Kapteyn, M. M. Murnane, L. Plaja, M. Lewenstein, C. Hernández-García, Conservation of torus-knot angular momentum in high-order harmonic generation. *Phys. Rev. Lett.* **122**, 203201 (2019).
19. E. Pisanty, G. J. Machado, V. Vicuña-Hernández, A. Picón, A. Celi, J. P. Torres, M. Lewenstein, Knotting fractional-order knots with the polarization state of light. *Nat. Photonics* **13**, 569–574 (2019).
20. S. Xu, C. Wu, Space-time crystal and space-time group. *Phys. Rev. Lett.* **120**, 096401 (2018).
21. T. Janssen, A. Janner, Aperiodic crystals and superspace concepts. *Acta Crystallogr. Sect. B Struct. Sci. Cryst. Eng. Mater.* **70**, 617–651 (2014).
22. V. S. Liu, B. K. Vanleeuwen, J. M. Munro, H. Padmanabhan, I. Dabo, V. Gopalan, D. B. Litvin, Spatio-temporal symmetry—Crystallographic point groups with time translations and time inversion. *Acta Crystallogr. Sect. A Found. Adv.* **74**, 399–402 (2018).
23. D. Shechtman, I. Blech, D. Gratias, J. W. Cahn, Metallic phase with long-range orientational order and no translational symmetry. *Phys. Rev. Lett.* **53**, 1951–1953 (1984).
24. R. Lifshitz, A. Arie, A. Bahabad, Photonic quasicrystals for nonlinear optical frequency conversion. *Phys. Rev. Lett.* **95**, 133901 (2005).
25. Z. V. Vardeny, A. Nahata, A. Agrawal, Optics of photonic quasicrystals. *Nat. Photonics* **7**, 177–187 (2013).
26. D. B. Litvin, W. Opechowski, Spin groups. *Phys. Ther.* **76**, 538–554 (1974).
27. N. V. B. Aleksei Vasil'evich Shubnikov, *Colored Symmetry* (Pergamon Press, 1964).
28. R. L. E. Schwarzenberger, Colour symmetry. *Bull. London Math. Soc.* **16**, 216–229 (1984).
29. M. R. Dennis, Polarization singularities in paraxial vector fields: Morphology and statistics. *Opt. Commun.* **213**, 201–221 (2002).
30. M. V. Berry, Index formulae for singular lines of polarization. *J. Opt. A Pure Appl. Opt.* **6**, 675–678 (2004).
31. G. Gariepy, J. Leach, K. T. Kim, T. J. Hammond, E. Frumker, R. W. Boyd, P. B. Corkum, Creating high-harmonic beams with controlled orbital angular momentum. *Phys. Rev. Lett.* **113**, 153901 (2014).
32. M. Lewenstein, P. Balcou, M. Y. Ivanov, A. L'Huillier, P. B. Corkum, Theory of high-harmonic generation by low-frequency laser fields. *Phys. Rev. A* **49**, 2117–2132 (1994).
33. Y. Tang, K. Li, X. Zhang, J. Deng, G. Li, E. Brasselet, Harmonic spin–orbit angular momentum cascade in nonlinear optical crystals. *Nat. Photonics* **14**, 658–662 (2020).
34. N. Wang, H. Chen, K. H. Kuo, Two-dimensional quasicrystal with eightfold rotational symmetry. *Phys. Rev. Lett.* **59**, 1010–1013 (1987).

35. L. Hareli, L. Lobachinsky, G. Shoulga, Y. Eliezer, L. Michaeli, A. Bahabad, On-the-fly control of high-harmonic generation using a structured pump beam. *Phys. Rev. Lett.* **120**, 183902 (2018).
36. O. Kfir, P. Grychtol, E. Turgut, R. Knut, D. Zusin, D. Popmintchev, T. Popmintchev, H. Nembach, J. M. Shaw, A. Fleischer, H. Kapteyn, M. Murnane, O. Cohen, Generation of bright phase-matched circularly-polarized extreme ultraviolet high harmonics. *Nat. Photonics* **9**, 99–105 (2014).
37. O. Kfir, E. Bordo, G. Ilan Haham, O. Lahav, A. Fleischer, O. Cohen, In-line production of a bi-circular field for generation of helically polarized high-order harmonics. *Appl. Phys. Lett.* **108**, 211106 (2016).
38. O. Neufeld, O. Cohen, Background-free measurement of ring currents by symmetry-breaking high-harmonic spectroscopy. *Phys. Rev. Lett.* **123**, 103202 (2019).
39. D. Ayuso, A. F. Ordonez, P. Decleva, M. Ivanov, O. Smirnova, Enantio-sensitive unidirectional light bending. *Nat. Commun.* **12**, 1–9 (2021).
40. C. Hernández-García, J. A. Pérez-Hernández, T. Popmintchev, M. M. Murnane, H. C. Kapteyn, A. Jaron-Becker, A. Becker, L. Plaja, Zeptosecond high harmonic keV X-ray waveforms driven by midinfrared laser pulses. *Phys. Rev. Lett.* **111**, 033002 (2013).
41. T. T. Luu, M. Garg, S. Y. Kruchinin, A. Moulet, M. T. Hassan, E. Goulielmakis, Extreme ultraviolet high-harmonic spectroscopy of solids. *Nature* **521**, 498–502 (2015).
42. J. Hamazaki, R. Morita, K. Chujo, Y. Kobayashi, S. Tanda, T. Omatsu, Optical-vortex laser ablation. *Opt. Express* **18**, 2144–2151 (2010).
43. K. Toyoda, K. Miyamoto, N. Aoki, R. Morita, T. Omatsu, Using optical vortex to control the chirality of twisted metal nanostructures. *Nano Lett.* **12**, 3645–3649 (2012).
44. S. Sederberg, F. Kong, F. Hufnagel, C. Zhang, E. Karimi, P. B. Corkum, Vectorized optoelectronic control and metrology in a semiconductor. *Nat. Photonics* **14**, 1–6 (2020).
45. T. S. Ho, S. I. Chu, J. V. Tietz, Semiclassical many-mode floquet theory. *Chem. Phys. Lett.* **96**, 464–471 (1983).
46. I. Martin, G. Refael, B. Halperin, Topological frequency conversion in strongly driven quantum systems. *Phys. Rev. X* **7**, 041008 (2017).
47. K. Drese, M. Holthaus, Floquet theory for short laser pulses. *Eur. Phys. J. D* **5**, 119–134 (1999).
48. C. Hernández-García, J. A. Pérez-Hernández, J. Ramos, E. C. Jarque, L. Roso, L. Plaja, High-order harmonic propagation in gases within the discrete dipole approximation. *Phys. Rev. A - At. Mol. Opt. Phys.* **82**, 033432 (2010).
49. L. Drescher, O. Kornilov, T. Witting, G. Reitsma, N. Monserud, A. Rouzée, J. Mikosch, M. J. J. Vrakking, B. Schütte, Extreme-ultraviolet refractive optics. *Nature* **564**, 91–94 (2018).
50. J. A. R. Samson, W. C. Stolte, Precision measurements of the total photoionization cross-sections of He, Ne, Ar, Kr, and Xe, in *Journal of Electron Spectroscopy and Related Phenomena* (Elsevier, 2002), vol. 123, pp. 265–276.
51. D. B. Litvin, *Magnetic Group Tables: 1-, 2- and 3-Dimensional Magnetic Subperiodic Groups and Magnetic Space Groups* (International Union of Crystallography, 2013).
52. R. Cireasa, A. E. Boguslavskiy, B. Pons, M. C. H. Wong, D. Descamps, S. Petit, H. Ruf, N. Thiré, A. Ferré, J. Suarez, J. Higuet, B. E. Schmidt, A. F. Alharbi, F. Légaré, V. Blanchet, B. Fabre, S. Patchkovskii, O. Smirnova, Y. Mairesse, V. R. Bhardwaj, Probing molecular chirality on a sub-femtosecond timescale. *Nat. Phys.* **11**, 654–658 (2015).
53. D. Baykusheva, H. J. Wörner, Chiral discrimination through bielliptical high-harmonic spectroscopy. *Phys. Rev. X* **8**, 031060 (2018).
54. O. Neufeld, M. Even Tzur, O. Cohen, Degree of chirality of electromagnetic fields and maximally chiral light. *Phys. Rev. A* **101**, 053831 (2020).

Acknowledgments

Funding: O.C. acknowledges support by the European Research Council (ERC) under the European Union's Horizon 2020 research and innovation programme (819440-TIMP). A.B. acknowledges support by the Israeli Science Foundation, grant no. 537/19. A.F. acknowledges support by the Israeli Science Foundation, grant no. 524/19. D.P. acknowledges support by the Israeli Science Foundation, grant no. 1803/18. O.N. acknowledges support of the Adams Fellowship Program of the Israel Academy of Sciences and Humanities, support from the Alexander von Humboldt foundation, and support from a Schmidt Science Fellowship. **Author contributions:** G.L., O.N., and O.C. initiated the research. G.L., O.N., A.F., and D.P. developed the theory. G.L. applied the theory to produce all the presented theoretical results. G.L., L.H., and G.S. conducted the experiment, supervised by A.B. G.L. and E.B. analyzed the experimental data. G.L., O.N., and O.C. wrote the first draft. All authors contributed to the writing the paper. O.C. supervised the project. **Competing interests:** The authors declare that they have no competing interests. **Data and materials availability:** All data needed to evaluate the conclusions in the paper are present in the paper and/or the Supplementary Materials.

Submitted 24 July 2022
Accepted 9 March 2023
Published 14 April 2023
10.1126/sciadv.ade0953

ScienceAdvances

Multiscale dynamical symmetries and selection rules in nonlinear optics

Gavriel Lerner, Ofer Neufeld, Liran Hareli, Georgiy Shoulga, Eliayu Bordo, Avner Fleischer, Daniel Podolsky, Alon Bahabad, and Oren Cohen

Sci. Adv., **9** (15), eade0953.
DOI: 10.1126/sciadv.ade0953